ACS APPLIED ELECTRONIC MATERIALS

pubs.acs.org/acsaelm

Article

Negative Capacitance Behavior at Low Frequencies of Nitrogen-Doped Polyethylenimine-Functionalized Graphene Quantum Dots-Based Structure

Zeynep Berktaş, Elif Orhan,* Murat Ulusoy, Mustafa Yildiz, and Şemsettin Altındal

Cite This: *ACS Appl. Electron. Mater.* 2023, 5, 1804−1811

Read Online

ACCESS | Metrics & More | Article Recommendations

ABSTRACT: Graphene quantum dots (GQDs), zero-dimensional members of the carbon family, have exceptional mechanical, thermal, and electrical properties. Nevertheless, pure GQDs have many challenges in reaching their full potential in electronic applications. Functionalizing or chemical modification of GQDs adjusts the physical and chemical properties, driving GQDs toward high-performance device applications. Nitrogen (N)-doped polyethylenimine (PEI) functionalized GQDs are capturing the interest of researchers specifically for electronic and photovoltaic applications these days. In this context, we present for the first time capacitance/conductance−voltage ($C-V$ and $G/\omega-V$) measurements of the nitrogen-doped PEI-functionalized GQDs-based structure for use in electronic applications in the frequency range from 1 kHz to 2 MHz at 300 K in this study. Capacitance features, the energy density distribution of surface states (N_{ss}), and the relaxation time (τ) of a nitrogen-doped PEI-functionalized GQDs-based structure have been examined by using the admittance/conductance method. Negative capacitance (NC) behavior mostly exhibited by ferroelectric materials has been observed in the GQDs-based structure at low frequencies, and then it starts to disappear. NC is usually attributed to various surface states/interface traps, series resistance (R_s), and minority carrier injection. The NC phenomenon indicates that an increase in voltage gives rise to a decrease in the charge on the electrodes. The control of interfacial charges in such a heterostructure will be critical for NC devices. The results provide a basis for insights into semiconductor device technology.

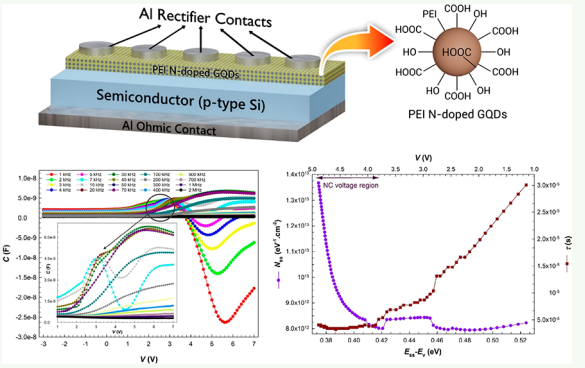

KEYWORDS: *graphene quantum dots (GQDs), nitrogen-doped polyethylenimine (PEI) functionalized GQDs, negative capacitance, energy-dependent profile of surface states, relaxation time*

1. INTRODUCTION

Graphene quantum dots (GQDs) are zero-dimensional (0D) members of the carbon family and consist of graphene nanoparticles.[1] GQDs possess many superiorities such as desired fluorescence properties,[2−4] good water solubility,[5] powerful electrochemical properties,[6,7] and low toxicity.[8,9] To date, GQDs have gained tremendous attention due to these properties for electronic, biological, sensing, and energy applications.[10−12] Among these applications, electronic and energy-related devices are rapidly rising.[13] GQDs can be an environmentally friendly, cost-effective, and more stable material for photovoltaics and photodiodes than current organic materials. The performance of GQDs-based devices can be further modified by selecting other polymers or different types of functionalization.[14,15] The functionalization of GQDs with complex-surface groups can improve the device performance in specific applications in facile methods and low cost. Nevertheless, doping of GQDs with heteroatoms such as sulfur (S),[16] nitrogen (N),[17,18] and other elements can ensure an increment in the electrical conductivity and luminescence by tuning their electronic structures.[19−21] There are several studies about nitrogen-doped GQDs (N-GQDs). For instance, Khan et al.[22] synthesized N-GQDs and embedded them in poly(methyl methacrylate) (PMMA) to improve the mechanical and chemical stability of luminescent photon downshifters (LDS). They reported enhancement in device performance. Gupta et al.[23] demonstrated that the GQDs dispersed in conjugated polymers show enhanced and organic photovoltaic (OPV) and organic light-emitting diode OLED characteristics. It has been seen that doping GQDs with heteroatoms[24] and

Received: January 3, 2023
Accepted: March 6, 2023
Published: March 16, 2023

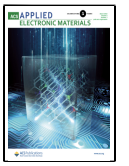

functionalizing them with polymers[14] has been shown to improve the photovoltaic performance of solar cells. Hasan et al.[25] and Dhar et al.[26] boosted UV photodetector performance by using N-GQDs. Also, when a little amount of PEI into several ambipolar and p-type polymer semiconductors in organic thin-film transistors was added, it was observed that PEI suppressed hole transport characteristics while promoting electron transport performance.[27] Although PEI-functionalized GQDs (PEI-GQDs) seem to be more preferred in research on biological applications, it has been observed that PEI-GQDs are also used in organic tandem solar cells and improve the performance of the device.[28] Tamal et al.[29] investigated the photovoltaic performance of N-GQDs. So far, studies with PEI-GQDs for electronic applications seem limited. There is also no study in the literature investigating the capacitance properties of PEI-GQDs structure. Capacitance features are very important for electronic applications. A capacitor is a crucial element of electronic devices and is represented by positive capacitance. However, in some cases, a negative capacitance (NC) behavior can happen and generally hints at local voltage drop across the applied bias. It has been seen that various ferroelectric-based micro/nanoelectronic devices have been developed with improved performance attributed to NC in the literature.[30] NC behavior in Schottky diodes (SDs) has been also reported by researchers.[31−33] NC means reducing the charge on the electrode by increasing the bias voltage. NC indicates that the products have inductive properties.[34] Electron hole recombination by local traps occurs via the NC effect.[35,36] Frequency-dependent admittance spectroscopy (G/ω−f) and C−f) data are used to define the NC. The frequency dependence of NC means that trap conditions dominate electron−hole recombination.[37−39] Ashery et al.[36] showed that the polypyrrole-based composite structure exhibited NC at low and high frequencies. Tu et al.[40] fabricated an ultrasensitive $MoS_2/Hf_{1-x}Zr_xO_2$ (x = 0.5) based phototransistor, which has the behavior of NC. Champness and Clark[39] noticed the NC behavior only at low frequencies and forward bias for the selenium Schottky diode. Song et al.[41] directly fabricated two-dimensional (2D) NiFe-metal−organic framework nanosheets (MOF NSs) induced by carboxylated carbon quantum dots (CQDs-COOH). They found excellent oxygen reduction reactions (ORR) and electrocatalytic performances to construct state-of-the-art energy conversion and storage devices. Zhang et al.[42] designed a simple two-step hydrothermal strategy to synthesize a highly efficient and excellent composite catalyst of monodisperse carbon dots (CDs) anchored on carbon nanotubes (CNTs). Zhang et al. obtained the excellent ORR that can be attributed to the dominant role of amino-N, the high Lewis basicity, and the synergistic effect of hetero-junctions formed by CNTs and CDs. Han et al.[43] introduced a machine learning (ML) strategy to successfully predict, optimize, and accelerate the CDs' synthesis process. The fabricated CDs can exhibit a strong green emission with quantum yields (QYs) of up to 39.3%. Wang et al.[44] fabricated a one-step acid reagent engineering strategy to acquire highly luminescent CQDs, having remarkably tunable and stable fluorescence emission from blue to red and even white light by using o-phenylenediamine (oPD) as the precursor. The relative photoluminescence (PL) quantum yields (QYs) of these CQDs reached 72%. Gokçen et al.[45] described the NC behavior for a SiO_2-based n-GaAs structure. The NC behavior on the C−V profile was attributed to the presence of N_{ss}, R_s, and minority carrier injection by Tanrıkulu et al.,[46] and Niu et al.[47] stated that an increase in electron trap density in bipolar organic diodes increased in NC. Joly et al.[48] observed NC values over a broad frequency range (20 Hz to 1 MHz). Al-Dharob et al.[49] measured temperature-dependent ($C/G/\omega$ /−V) properties of a metal−polymer−semiconductor structure and observed NC behavior. The NC behavior in the nitrogen-doped PEI-functionalized GQDs structure was presented for the first time by us in this study.

In this study, we fabricated a new type of nitrogen-doped PEI-functionalized GQDs-based SD instead of classic metal/insulator/semiconductor (MIS)-type SDs. C/G-V and C/G-f measurements were performed over a broad frequency range (1 kHz to 2 MHz) for voltages ranging from −3 to 7 V at 300 K.

2. EXPERIMENTAL METHODS

2.1. Synthesis and Characterization of Nitrogen-Doped PEI-Functionalized GQDs. In this study, we preferred a hydrothermal process to synthesize nitrogen-doped PEI-functionalized GQDs. Citric acid (CA) was used as a source of carbon. N-doped PEI-GQDs were synthesized in an autoclave aqueous medium via the hydrothermal reaction of CA and PEI.[50] The steps of the synthesis of nitrogen-doped PEI-functionalized GQDs were given in our previous work.[50]

Infrared absorption spectra of GQDs were obtained from a PerkinElmer BX II Fourier Transform Infrared (FT-IR) Spectrometer in KBr discs and were reported in cm^{-1} units. PEI-functionalized N-doped GQDs were morphologically characterized by transmission electron microscopy (TEM) (FEI Technai G2 STwin) at an accelerating voltage of 200 kV. The materials in aqueous suspensions were treated in an ultrasonic bath before dropping to reduce aggregation. A 10 μL aliquot of distributed nanostructures was dropped on Formvar/carbon-coated 200 mesh copper grids and dried under ambient conditions. Elemental compositions of the N-doped PEI GQDs materials were analyzed using energy-dispersive X-ray spectroscopy (EDX) (Bruker AXs XFlash Detector 4010).

2.2. Production of Al (Nitrogen-Doped PEI-Functionalized GQDs)/p-Si Schottky Diode. For creating the diode structure, we used p-type Si (100) as a wafer. Cleaning procedures[51,52] were applied to a p-type Si wafer. As aluminum (Al) contacts are widely used to form both ohmic and rectifying contacts, an Al ohmic contact was deposited with a thickness of 248 nm on the unpolished side of the p-type Si wafer via the physical vapor deposition technique (PVD). A concentrated solution of N-doped PEI-functionalized GQDs was prepared in ultrapure water. The N-doped PEI-GQDs solution was deposited on the polished p-Si wafer by using a spin-coating technique. The spin-coating speed is 3000 rpm, and the spin-coating time was locked for 30 s. The film thickness is ∼26 nm. Finally, 128 nm thick Al contacts were formed on N-doped PEI-functionalized GQDs via the thermal evaporation technique by using a 1 mm diameter circular metal mask. The structure of the N-doped PEI-functionalized GQDs-based Schottky diode was given in Figure 1 as a representative.

3. RESULTS AND DISCUSSION

We present a study about capacitance and conductance (C, G/ω) measurements of a GQDs-based diode functionalized with PEI polymer and nitrogen in a wide frequency range at room temperature. In this study, firstly the f N-doped PEI-functionalized GQDs nanostructures synthesized by the hydrothermal method was characterized by FT-IR, TEM, and EDX.

The FT-IR spectrum of N-doped PEI GQDs shows characteristic changes in functional group frequencies compared to the spectra of the starting materials CA and

https://doi.org/10.1021/acsaelm.3c00011
ACS Appl. Electron. Mater. 2023, 5, 1804−1811

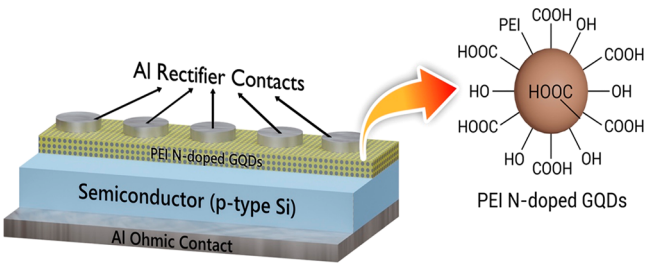

Figure 1. Shematic representation of nitrogen-doped PEI-functionalized GQDs-based Schottky diode.

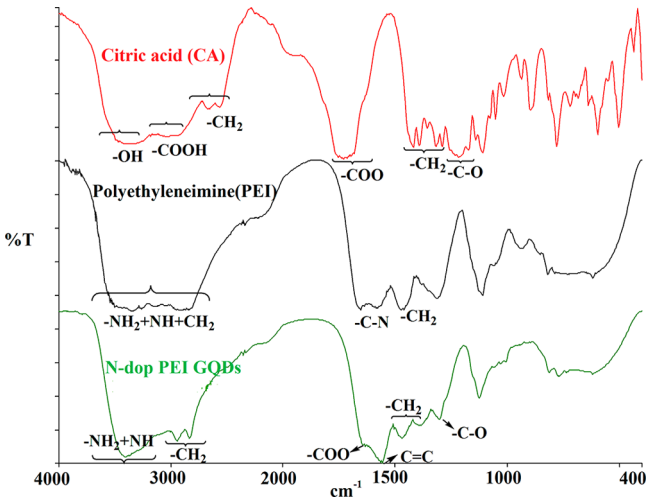

Figure 2. FTIR spectra of the nitrogen-doped PEI-functionalized GQDs and starting materials.

PEI (Figure 2). The OH+COOH, C−H (aliphatic), C═O, and −C−O vibrational bands are observed at 3410 (broad), 2945, 2837, 1557, 1471, 1647, and 1392 cm^{-1}, respectively, in the starting material CA. In the FTIR spectrum of the starting compound PEI, characteristic NH_2+NH+CH_2 vibrations are observed over a wide region at 3535, 3344, and 2920 cm^{-1}, respectively, and these bands overlap. Again in PEI spectra, the bands observed at 1654 cm^{-1} and at 1584, 1474, and 1318 cm^{-1} belong to −C−N− and $-CH_2$ vibrations, respectively.

Accordingly, OH+NH_2+NH+COOH+C−H (aromatic) vibrations are observed to overlap at 3373 cm^{-1} in the FTIR spectrum of N-doped PEI functional GQDs. Aliphatic-H vibrations are found at 2670−2568 cm^{-1}. The functional and aliphatic-H groups vibrate in the material at a lower frequency than the starting compounds. In N-doped PEI functional GQDs, C═O, C═C, and C−N vibrations are observed as a very strong band at 1730 and 1682 cm^{-1}, respectively. The C═C and C−N bands in the material are found to overlap. The C═O vibration is shifted to a very high frequency relative to the output compound CA. Aliphatic CH_2 vibrations are found at 1419−1392−137−57 cm^{-1}, and C−O vibrations are found at 1319 cm^{-1}.

The N-doped PEI functional GQDs morphology and structure were also confirmed by its TEM image as shown in Figure 3a. The TEM analysis verifies the presence of the material (particle sizes; 9−17 nm). Also, the additional characterization was performed by TEM with the EDX detector (Figure 3b). Figure 3b shows the amounts of elements detected by using the EDX method; nitrogen, carbon, and oxygen were observed on the surface of samples.

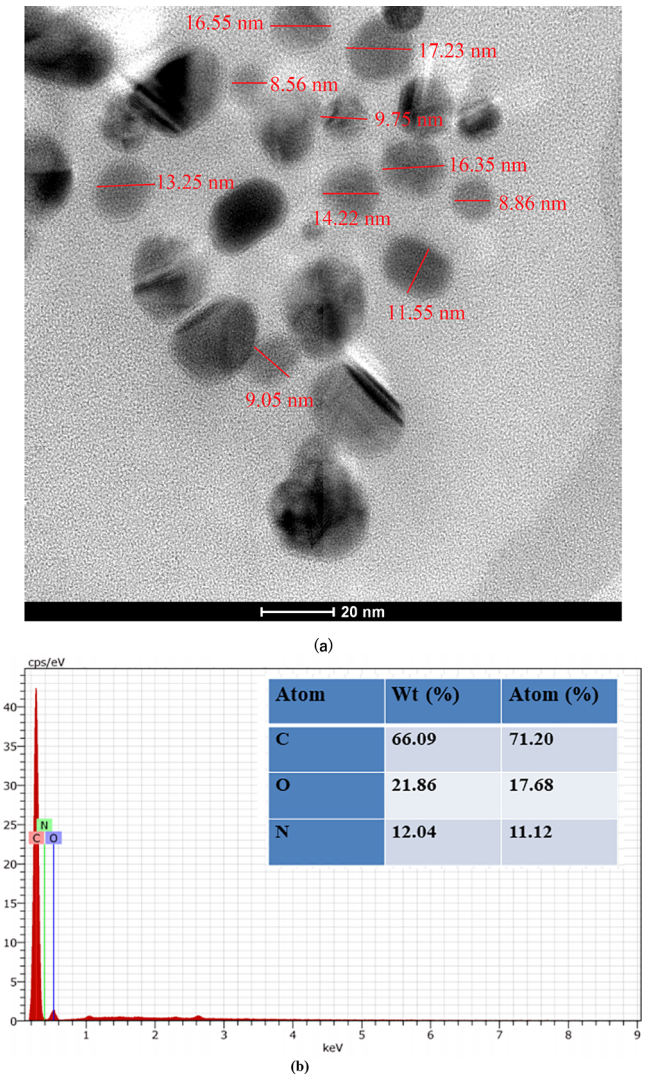

Figure 3. (a) TEM image and (b) EDX spectrum of of nitrogen-doped PEI-functionalized GQDs.

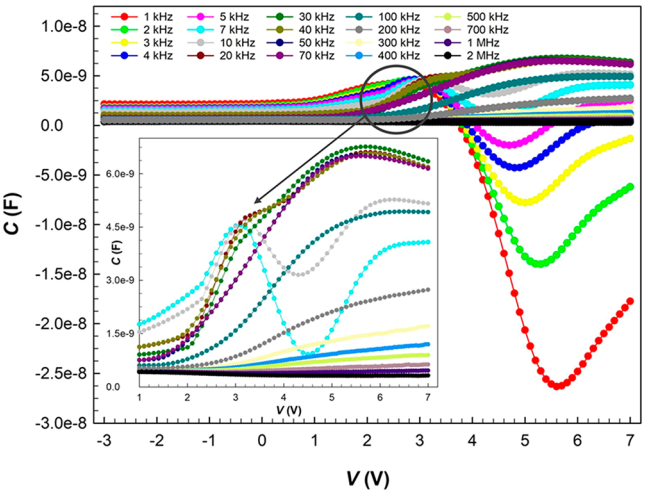

Figure 4. *C*−*V* plots of the structure in the frequency range from 1 kHz to 2 MHz.

However, EDX only detects elements on the surface. It never gives a complete elemental analysis. In addition, EDX data

https://doi.org/10.1021/acsaelm.3c00011
ACS Appl. Electron. Mater. 2023, 5, 1804−1811

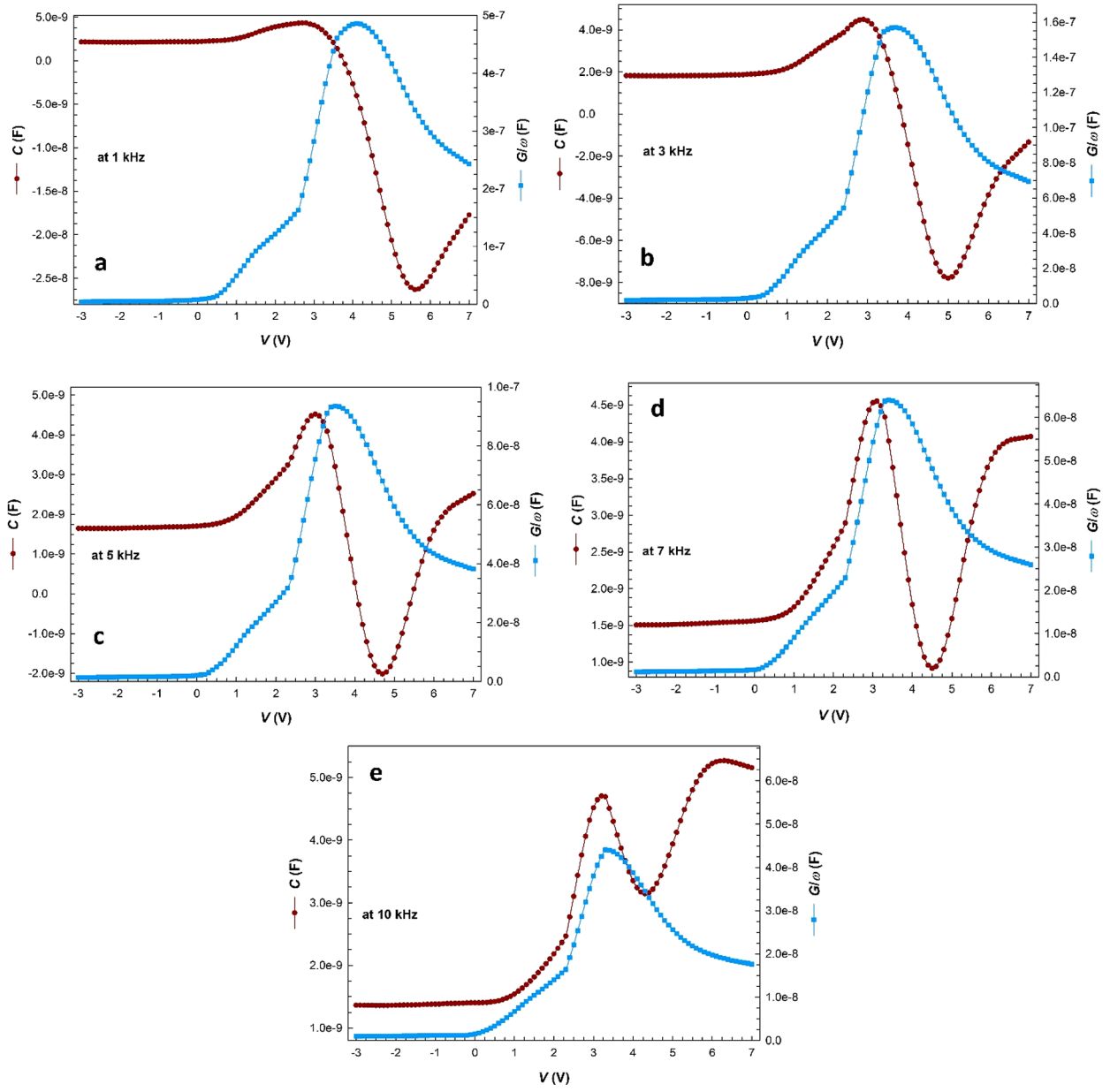

Figure 5. $C-V$ curves of the structure at (a) 1, (b) 3, (c) 5, (d) 7, and (e) 10 kHz.

confirm the presence of nitrogen in N-doped GQDs. This result proves that N-doped GQDs occur.

The $C-V$ and $G/\omega-V$ features of the nitrogen-doped PEI-functionalized GQDs-based SD were performed for various frequencies from 1 kHz to 2 MHz and between −3 and 7 V. $C-V$ plots of this structure in the frequency range from 1 kHz to 2 MHz were given in Figure 4. Figure 4 revealed NC behavior at low frequencies. It has been observed that, when the frequency drops below 7 kHz, the capacitance goes to a negative value. The curves $C/G/\omega-V$ of the nitrogen-doped PEI-functionalized GQDs-based SD for low frequencies (1, 3, 5, 7, and 10 kHz) were also embedded in Figure 5 to see NC and inductive behavior. As seen in Figure 5, the NC has a maximum value at 1 kHz, and above 7 kHz, the NC disappears. Moreover, as can be seen in Figure 4a−e, the minimum value of C corresponds to the maximum value of G/ω, which is known as a "conductive behavior" in the literature.[38,39,46] The reason for NC is usually rooted in various sources such as surface states/interface traps or dislocations and their specific life/relaxation times, R_s, and minority carrier injection.

The $G/\omega-V$ plots of the nitrogen-doped PEI-functionalized GQDs-based SD were also given in Figure 6 for various frequency ranges (1 kHz−2 MHz). As can be seen in Figures 4 and 6, the $C-V$ and $G/\omega-V$ plots have three regions as accumulation, depletion, and inversion of the structure, respectively. In addition, both the values of C and G/ω are a strong function of frequency, especially in depletion and accumulation regions, but while surface states are effective in the depletion region, R_s and the interfacial layer are effective in the accumulation region. As the electric field increases and the interfacial traps fill, the electrons gain more energy and collide with the electrons trapped in the interfacial states below the Fermi level at the metal−semiconductor (MS) junction and carry them to the semiconductor valence band. Therefore, N_{ss} has an important role in the impedance measurements and NC behavior and an anomalous peak in the $C-V$ and $G/\omega-V$

https://doi.org/10.1021/acsaelm.3c00011
ACS Appl. Electron. Mater. 2023, 5, 1804−1811

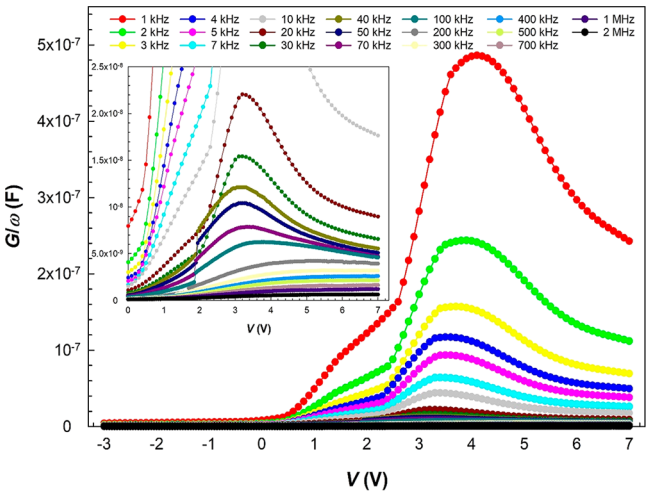

Figure 6. $G/\omega-V$ plots of the structure.

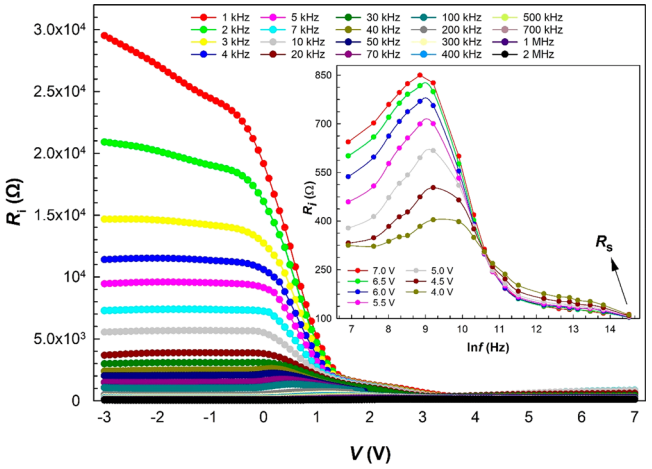

Figure 7. R_i-V curves of the structure in the frequency range from 1 kHz to 2 MHz.

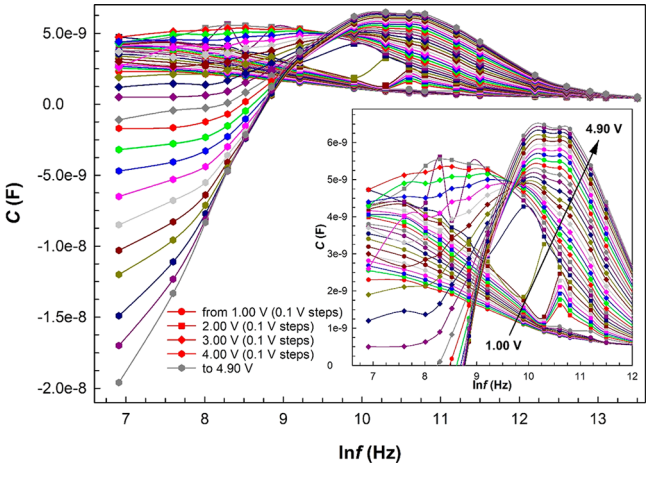

Figure 8. $C-\ln f$ curves of the structure between 1 and 4.9 V.

plots, especially at low frequencies in MS and MIS-type structures.[48] When looking at high frequencies, no significant increase in capacitance values was observed because the charges at the interface cannot follow the AC signal and so can not contribute to the real values of C and G/ω. This is because

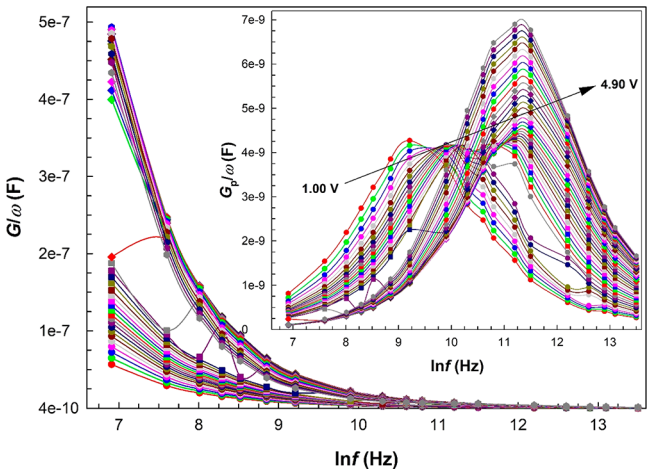

Figure 9. $G/\omega-\ln f$ curves of the structure between 1 and 4.9 V.

they have a lifetime (τ) higher than $1/\omega$ ($\omega = 2\pi f = 2\pi/T$ is angular frequency).

The other critical parameter for MS or MIS-type structures is the R_s of them especially at high frequency at the accumulation region, which leads to a concave curvature in the $C-V$ plots or an anomalous peak. Therefore, the voltage-dependent profile of R_i is determined by the Nicollian and Brews method for each frequency.[53] According to this method, R_i at high frequencies is considered the real value of R_s. Therefore, the real value of R_s has been calculated by the measured capacitance and conductance at the strong accumulation region (C_m and G_{ma}). But, the value of resistance (R_i) can be calculated from the C_m and G_m data for each bias voltage by using eq 1. According to eq 1, R_s is inversely proportional to G_m.

$$R_i = \frac{G_m}{G_m^2 + (\omega C_m)^2} \tag{1}$$

Thus, the R_i-V graph was obtained from eq 1 for each frequency and presented in Figure 7 for different frequencies at room temperature. As can be seen in Figure 7, at the accumulation region, the decrease in R_i at high frequencies is due to the increase in conductivity. As can be seen in the inset of Figure 6, the observed peaks are in the R_i versus V plots. This is the result of a special density distribution of surface states and restructures/reordering of them under an electric field. In addition, the decrease of the R_s at the accumulation region is the result of increasing conductance. The value of R_i becomes almost constant at a strong accumulation region, which corresponds to the real value of R_s at high frequency. There are several methods to calculate the voltage- or energy-dependent profile of N_{ss} such as Hill-Coleman, low-high frequency capacitance, admittance, or parallel conductance.[53−56] However, the admittance method is the most reliable and sensitive one among them so the following relation (eq 2) is used[53]

$$\frac{G_p}{\omega} = \frac{\omega G_m C_i}{G_m^2 + \omega^2 (C_i - C_m)^2} = \frac{qAN_{ss}}{2\omega\tau}\ln(1 + (\omega\tau)^2) \tag{2}$$

where C_i is the interfacial layer capacitance, C_m and G_m are the measurement capacitance and conductance values, A is the rectifier-contact area, and τ is the relaxation time. To determine both the value of N_{ss} and their lifetimes, first,

https://doi.org/10.1021/acsaelm.3c00011
ACS Appl. Electron. Mater. 2023, 5, 1804−1811

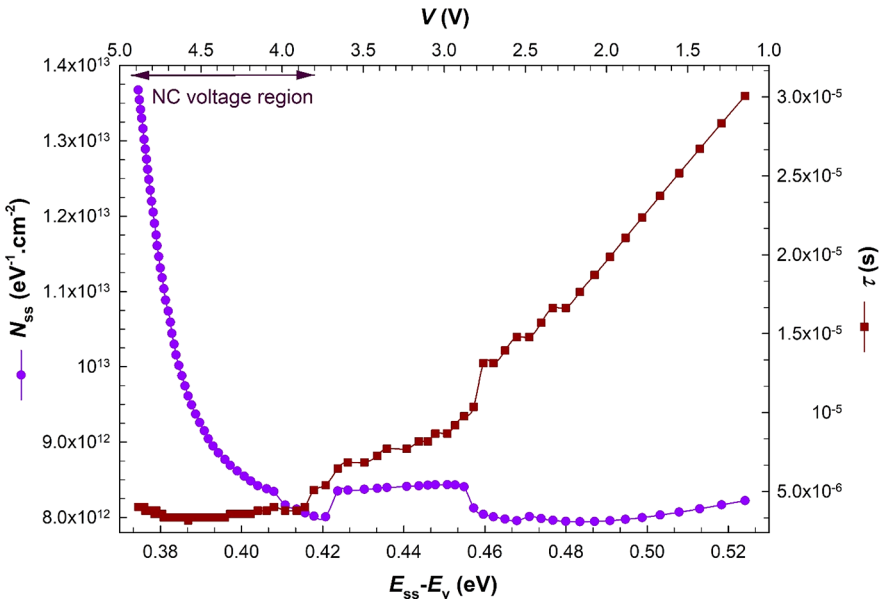

Figure 10. Energy distribution characteristic of the N_{ss} and τ for nitrogen-doped PEI-functionalized GQDs-based Schottky diode.

both the $C-\ln f$ and $G/\omega-\ln f$ curves of the structure were drawn between 1.0 and 4.9 V by 0.1 V steps and presented in Figure 8. As can be seen in this figure, both the values of C and G/ω usually decrease with an increasing frequency almost exponentially. There are peaks in the $C-\ln f$ graph, which is due to the distribution of interface states and the presence of different frequencies corresponding to each interface. After that, the $G_p/\omega-\ln f$ plots were obtained from eq 2 and presented in Figure 9. Due to the characteristic distribution of N_{ss} and relaxation times, the peaks were observed to shift toward higher frequencies. The N_{ss} value in eq 2 is found using the derivative operation. When the derivative of the eq concerning $\omega\tau$ is zero at each vertex, the value of $\omega\tau$ is 1.98.

Thus, the values of N_{ss} and τ were determined from the peak value of the G_p/ω versus f plot by using the following relations.[53−56]

$$N_{ss} = \frac{(G_p/\omega)_{max}}{0.402qA} \quad (3)$$

$$\omega\tau = 1.98 \quad (4)$$

In the peak values of the G_p/ω, $\omega\tau$ = 1.98, and so the relaxation time is equal to $1.98/\omega$. Thus, the obtained energy-dependent values of N_{ss} and τ of the nitrogen-doped PEI-functionalized GQDs-based SD at room temperature were given in Figure 10. As can be seen in Figure 10, while the N_{ss} versus $E_{ss}-E_v$ plot has almost a U-shape behavior, the value of τ increases from the near valence band to the midgap gap of Si. Besides, the interface states were found to be concentrated in the NC voltage region. The obtained mean N_{ss} values at about 8×10^{12} eV^{-1} cm^{-2} are very suitable when compared to MS-type SDs.

4. CONCLUSION

We present a study about capacitance and conductance measurements of GQDs with a nitrogen-doped and functionalized PEI polymer-based diode at a frequency range from 1 kHz to 2 MHz in the voltage range from −3 to +7 V. NC behavior has been observed in the nitrogen-doped PEI-functionalized GQDs-based SD at low frequencies. The reason for the NC is related to the fact that there are various interface states with different lifetimes corresponding to each low and intermediate frequency. Inductive behavior was seen at low-frequency values, which is when the value of C starts to decrease and G increases. At the accumulation region, the decrease in R_i at high frequencies is due to the increase in conductivity. The observed peak at $C-V$ and $G/\omega-V$ plots was owing to a special distribution of surface states and their restructure and reordering under an electric field effect. While the N_{ss} versus $E_{ss}-E_v$ plot has almost a U-shape behavior, the value of τ increases from the near valence band to the midgap gap of Si due to a special density distribution of N_{ss} in the energy bandgap near the junction. The obtained values of N_{ss} at about 8×10^{12} eV^{-1} cm^{-2} are very suitable when compared to MS-type SDs. Consequently, the control of interfacial charges in such a heterostructure will be critical for NC devices. The results provide a basis for insights into semiconductor device technology.

AUTHOR INFORMATION

Corresponding Author

Elif Orhan − *Department of Physics, Gazi University, 06500 Ankara, Turkey;* orcid.org/0000-0002-3949-6141; Phone: +90312 202 1263; Email: eliforhan@gazi.edu.tr

Authors

Zeynep Berktaş − *Department of Advanced Technologies, Gazi University, 06500 Ankara, Turkey*

Murat Ulusoy − *Department of Physics, Gazi University, 06500 Ankara, Turkey*

Mustafa Yildiz − *Department of Chemistry, Çanakkale Onsekiz Mart University, 17100 Çanakkale, Turkey*

Şemsettin Altındal − *Department of Physics, Gazi University, 06500 Ankara, Turkey*

Complete contact information is available at: https://pubs.acs.org/10.1021/acsaelm.3c00011

Notes

The authors declare no competing financial interest.

https://doi.org/10.1021/acsaelm.3c00011
ACS Appl. Electron. Mater. 2023, 5, 1804−1811

■ ACKNOWLEDGMENTS

The authors gratefully acknowledge the Scientific Research Council (BAP) of Gazi University for the financial support of this research through Project No. FGA-2022-8252. The authors would like to thank the Photonics Application and Research Center of Gazi University.

■ REFERENCES

(1) Benítez-Martínez, S.; Valcárcel, M. Graphene quantum dots in analytical science. *TrAC - Trends Anal Chem.* **2015**, *72*, 93−113.
(2) Carrasco, P. M.; García, I.; Yate, L.; Tena Zaera, R.; Cabañero, G.; Grande, H. J.; Ruiz, V. Graphene quantum dot membranes as fluorescent sensing platforms for Cr (VI) detection. *Carbon N Y* **2016**, *109*, 658−65.
(3) Reagen, S.; Wu, Y.; Liu, X.; Shahni, R.; Bogenschuetz, J.; Wu, X.; Chu, Q. R.; Oncel, N.; Zhang, J.; Hou, X.; Combs, C.; Vasquez, A.; Zhao, J. X. Synthesis of Highly Near-Infrared Fluorescent Graphene Quantum Dots Using Biomass-Derived Materials for in Vitro Cell Imaging and Metal Ion Detection. *ACS Appl. Mater. Interfaces* **2021**, *13*, 43952−62.
(4) Wang, Z.; Zeng, H.; Sun, L. Graphene quantum dots: Versatile photoluminescence for energy, biomedical, and environmental applications. *J. Mater. Chem. C* **2015**, *3*, 1157−65.
(5) Kumar, G. S.; Thupakula, U.; Sarkar, P. K.; Acharya, S. Easy extraction of water-soluble graphene quantum dots for light emitting diodes. *RSC Adv.* **2015**, *5*, 27711−6.
(6) Li, Y.; Shu, H.; Niu, X.; Wang, J. Electronic and Optical Properties of Edge-Functionalized Graphene Quantum Dots and the Underlying Mechanism. *J. Phys. Chem. C* **2015**, *119*, 24950−7.
(7) Huang, Y.; Cheng, H.; Shi, G.; Qu, L. Highly Efficient Moisture-Triggered Nanogenerator Based on Graphene Quantum Dots. *ACS Appl. Mater. Interfaces* **2017**, *9*, 38170−5.
(8) Kuo, W.-S.; Chen, H.-H.; Chen, S.-Y.; Chang, C.-Y.; Chen, P.-C.; Hou, Y.-I; Shao, Y.-T.; Kao, H.-F.; Lilian Hsu, C.-L.; Chen, Y.-C.; Chen, S.-J.; Wu, S.-R.; Wang, J.-Y. Graphene quantum dots with nitrogen-doped content dependence for highly efficient dual-modality photodynamic antimicrobial therapy and bioimaging. *Biomaterials* **2017**, *120*, 185−194.
(9) Zhang, F.; Liu, F.; Wang, C.; Xin, X.; Liu, J.; Guo, S.; Zhang, J. Effect of Lateral Size of Graphene Quantum Dots on Their Properties and Application. *ACS Appl. Mater. Interfaces* **2016**, *8*, 2104−10.
(10) Zhu, J.; Tang, Y.; Wang, G.; Mao, J.; Liu, Z.; Sun, T.; Wang, M.; Chen, D.; Yang, Y.; Li, J.; Deng, Y.; Yang, S. Green, Rapid, and Universal Preparation Approach of Graphene Quantum Dots under Ultraviolet Irradiation. *ACS Appl. Mater. Interfaces* **2017**, *9*, 14470−7.
(11) Ghaffarkhah, A.; Hosseini, E.; Kamkar, M.; Sehat, A. A.; Dordanihaghighi, S.; Allahbakhsh, A.; Kuur, C.; Arjmand, M. Synthesis, Applications, and Prospects of Graphene Quantum Dots: A Comprehensive Review. *Small* **2022**, *18*, 18.
(12) Hosseini, Z. S.; Iraji Zad, A.; Ghiass, M. A.; Fardindoost, S.; Hatamie, S. A new approach to flexible humidity sensors using graphene quantum dots. *J. Mater. Chem. C* **2017**, *5*, 8966−73.
(13) Younis, M. R.; He, G.; Lin, J.; Huang, P. Recent Advances on Graphene Quantum Dots for Bioimaging Applications. *Front Chem.* **2020**, *8*, 1−25.
(14) Mahalingam, S.; Manap, A.; Omar, A.; Low, F. W.; Afandi, N. F.; Chia, C. H.; Rahim, N. A. Functionalized graphene quantum dots for dye-sensitized solar cell: Key challenges, recent developments and future prospects. *Renew Sustain Energy Rev.* **2021**, *144*, 110999.
(15) Zhang, L.; Xu, H.; Ding, Z.; Hu, J.; Liu, J.; Liu, Y. Amino: N -oxide functionalized graphene quantum dots as a cathode interlayer for inverted polymer solar cells. *J. Mater. Chem. C* **2018**, *6*, 5684−9.
(16) Dong, Y.; Pang, H.; Yang, H. B.; Guo, C.; Shao, J.; Chi, Y.; Li, C. M.; Yu, T. Carbon-based dots co-doped with nitrogen and sulfur for high quantum yield and excitation-independent emission. *Angew. Chemie - Int. Ed* **2013**, *52*, 7800−4.
(17) Hu, C.; Liu, Y.; Yang, Y.; Cui, J.; Huang, Z.; Wang, Y.; Yang, L.; Wang, H.; Xiao, Y.; Rong, J. One-step preparation of nitrogen-doped graphene quantum dots from oxidized debris of graphene oxide. *J. Mater. Chem. B* **2013**, *1*, 39−42.
(18) Zhu, C.; Yang, S.; Wang, G.; Mo, R.; He, P.; Sun, J.; Di, Z.; Yuan, N.; Ding, J.; Ding, G.; Xie, X. Negative induction effect of graphite N on graphene quantum dots: Tunable band gap photoluminescence. *J. Mater. Chem. C* **2015**, *3*, 8810−6.
(19) Ananthanarayanan, A.; Wang, Y.; Routh, P.; Sk, M. A.; Than, A.; Lin, M.; Zhang, J.; Chen, J.; Sun, H.; Chen, P. Nitrogen and phosphorus co-doped graphene quantum dots: Synthesis from adenosine triphosphate, optical properties, and cellular imaging. *Nanoscale* **2015**, *7*, 8159−65.
(20) Kundu, S.; Yadav, R. M.; Narayanan, T. N.; Shelke, M. V.; Vajtai, R.; Ajayan, P. M.; Pillai, V. K. Synthesis of N, F and S co-doped graphene quantum dots. *Nanoscale* **2015**, *7*, 11515−9.
(21) Feng, J.; Dong, H.; Pang, B.; Chen, Y.; Yu, L.; Dong, L. Tuning the electronic and optical properties of graphene quantum dots by selective boronization. *J. Mater. Chem. C* **2019**, *7*, 237−46.
(22) Khan, F.; Alshahrani, T.; Fareed, I.; Al-Rasheidi, M.; Ahmad, N.; Al-Ahmed, A.; Zahir, M. H.; Kim, J. H. Impact of solvent on the downconversion efficiency of the N-GQDs/PMMA layer: Application in CIGS solar cells. *Optik (Stuttg)* **2022**, *253*, 168569.
(23) Gupta, V.; Chaudhary, N.; Srivastava, R.; Sharma, G. D.; Bhardwaj, R.; Chand, S. Luminscent graphene quantum dots for organic photovoltaic devices. *J. Am. Chem. Soc.* **2011**, *133*, 9960−3.
(24) Hasan, T.; Gonzalez-rodriguez, R.; Ryan, C.; Pota, K.; Green, K.; Coffer, J. L.; Naumov, A. V. Nitrogen-doped graphene quantum dots : Optical properties modification and photovoltaic applications. *Nano Res.* **2019**, *12*, 1041−1047.
(25) Hasan, M. T.; Gonzalez-Rodriguez, R.; Ryan, C.; Coffer, J. L.; Naumov, A. V. Variation of Optical Properties of Nitrogen-doped Graphene Quantum Dots with Short/Mid/Long-wave Ultraviolet for the Development of the UV Photodetector. *ACS Appl. Mater. Interfaces* **2019**, *11*, 39035−45.
(26) Dhar, S.; Majumder, T.; Chakraborty, P.; Mondal, S. P. DMSO modified PEDOT:PSS polymer/ZnO nanorods Schottky junction ultraviolet photodetector: Photoresponse, external quantum efficiency, detectivity, and responsivity augmentation using N doped graphene quantum dots. *Org. Electron* **2018**, *53*, 101−10.
(27) Sun, B.; Hong, W.; Thibau, E. S.; Aziz, H.; Lu, Z. H.; Li, Y. Polyethylenimine (PEI) As an Effective Dopant to Conveniently Convert Ambipolar and p-Type Polymers into Unipolar n-Type Polymers. *ACS Appl. Mater. Interfaces* **2015**, *7*, 18662−71.
(28) Ho, N. T.; Tam, T. V.; Tien, H. N.; Jang, S.-J.; Nguyen, T. K.; Choi, W. M.; Cho, S.; Kim, Y. S. Solution-Processed Transparent Intermediate Layer for Organic Tandem Solar Cell Using Nitrogen-Doped Graphene Quantum Dots. *J. Nanosci Nanotechnol* **2017**, *17*, 5686−5692.
(29) Dey, T.; Ghorai, A.; Das, S.; Ray, S. K. Solvent-engineered performance improvement of graphene quantum dot sensitized solar cells with nitrogen functionalized GQD photosensitizers. *Sol Energy* **2022**, *236*, 17−25.
(30) Íñiguez, J.; Zubko, P.; Luk'yanchuk, I.; Cano, A. Ferroelectric negative capacitance. *Nat. Rev. Mater.* **2019**, *4*, 243−56.
(31) Ershov, M.; Liu, H. C.; Li, L.; Buchanan, M.; Wasilewski, Z. R.; Jonscher, A. K. Negative capacitance effect in semiconductor devices. *IEEE Trans. Electron Devices* **1998**, *45*, 2196−206.
(32) Perera, A. G. U.; Shen, W. Z.; Ershov, M.; Liu, H. C.; Buchanan, M.; Schaff, W. J. Negative capacitance of GaAs homojunction far-infrared detectors. *Appl. Phys. Lett.* **1999**, *74*, 3167−9.
(33) Ma, J.-G.; Yeo, K. S.; Do, M. A. Comments on "negative capacitance effect in semiconductor devices.". *IEEE Trans Electron Devices* **1999**, *46*, 2357−2358.
(34) Zhu, C. Y.; Feng, L. F.; Wang, C. D.; Cong, H. X.; Zhang, G. Y.; Yang, Z. J.; Chen, Z. Z. Negative capacitance in light-emitting devices. *Solid-State Electron.* **2009**, *53*, 324−8.
(35) Fedotova, J. A.; Pashkevich, A. V.; Ronassi, A. A.; Kołtunowicz, T. N.; Fedotov, A. K.; Zukowski, P.; Fedotov, A. S.; Kasiuk, J. V.; Kalinin, Y. E.; Sitnikov, A. V.; Fedotova, V. V.; Evtuh, A. Negative

https://doi.org/10.1021/acsaelm.3c00011
ACS Appl. Electron. Mater. 2023, 5, 1804−1811

capacitance of nanocomposites with CoFeZr nanoparticles embedded into silica matrix. *J. Magn Magn Mater.* **2020**, *511*, 511.
(36) Ashery, A.; Gaballah, A. E. H.; M Ahmed, E. Novel negative capacitance, conductance at high and low frequencies in Au/Polypyrrole-MWCNT composite /TiO_2/Al_2O_3/n-Si structure. *Mater. Res. Express* **2021**, *8*, 8.
(37) Lungenschmied, C.; Ehrenfreund, E.; Sariciftci, N. S. Negative capacitance and its photo-inhibition in organic bulk heterojunction devices. *Org. Electron* **2009**, *10*, 115−8.
(38) Guclu, C.S.; Ozdemir, A.F.; Karabulut, A.; Kokce, A.; Altındal, S. Investigation of temperature dependent negative capacitance in the forward bias C-V characteristics of (Au/Ti)/Al2O3/n-GaAs Schottky barrier diodes (SBDs). *Mater. Sci. Semicond Process* **2019**, *89*, 26−31.
(39) Champness, C. H.; Clark, W. R. Anomalous inductive effect in selenium Schottky diodes. *Appl. Phys. Lett.* **1990**, *56*, 1104−6.
(40) Tu, L.; Cao, R.; Wang, X.; Chen, Y.; Wu, S.; Wang, F.; Wang, Z.; Shen, H.; Lin, T.; Zhou, P.; Meng, X.; Hu, W.; Liu, Q.; Wang, J.; Liu, M.; Chu, J. Ultrasensitive negative capacitance phototransistors. *Nat. Commun.* **2020**, *11*, 4−11.
(41) Song, D.; Guo, H.; Huang, K.; Zhang, H.; Chen, J.; Wang, L.; Lian, C.; Wang, Y. Carboxylated carbon quantum dot-induced binary metal−organic framework nanosheet synthesis to boost the electrocatalytic performance. *Mater. Today* **2022**, *54*, 42−51.
(42) Zhang, B.; An, G.; Chen, J.; Guo, H.; Wang, L. Surface state engineering of carbon dot/carbon nanotube heterojunctions for boosting oxygen reduction performance. *J. Colloid Interface Sci.* **2023**, *637*, 173.
(43) Han, Y.; Tang, B.; Wang, L.; Bao, H.; Lu, Y.; Guan, C.; Zhang, L.; Le, M.; Liu, Z.; Wu, M. Machine-learning-driven synthesis of carbon dots with enhanced quantum yields. *ACS Nano* **2020**, *14*, 14761−8.
(44) Wang, L.; Li, W.; Yin, L.; Liu, Y.; Guo, H.; Lai, J.; Han, Y.; Li, G.; Li, M.; Zhang, J.; Vajtai, R.; Ajayan, P. M.; Wu, M. Full-color fluorescent carbon quantum dots. *Sci. Adv.* **2020**, *6*, 1−9.
(45) Gokcen, M.; Tunc, T.; Altındal, S.; Uslu, I. Electrical and photocurrent characteristics of Au/PVA (Co-doped)/n-Si photoconductive diodes. *Mater. Sci. Eng. B Solid-State Mater. Adv. Technol.* **2012**, *177*, 416−20.
(46) Tanrıkulu, E. E.; Demirezen, S.; Altındal, S.; Uslu, I. On the anomalous peak and negative capacitance in the capacitance−voltage (C−V) plots of Al/(%7 Zn-PVA)/p-Si (MPS) structure. *J. Mater. Sci. Mater. Electron* **2018**, *29*, 2890−2898.
(47) Niu, Q.; Craciun, N. I.; Wetzelaer, G.-J. A. H.; Blom, P. W. M. Origin of Negative Capacitance in Bipolar Organic Diodes. *Phys. Rev. Lett.* **2018**, *120*, 1−5.
(48) Joly, R.; Girod, S.; Adjeroud, N.; Grysan, P.; Polesel-maris, J. Evidence of negative capacitance and capacitance modulation by light and mechanical stimuli in pt/zno/pt schottky junctions. *Sensors* **2021**, *21*, 2253.
(49) Al-Dharob, M. H.; Kökce, A.; Aldemir, D. A.; Özdemir, A. F.; Altındal, Ş. The origin of anomalous peak and negative capacitance on dielectric behavior in the accumulation region in Au/(0.07 Zn-doped polyvinyl alcohol)/n-4H−SiC metal-polymer-semiconductor structures/diodes studied by temperature-dependent impedance measurements. *J. Phys. Chem. Solids* **2020**, *144*, 144.
(50) Berktaş, Z.; Yıldız, M.; Seven, E.; Oz Orhan, E.; Altındal, Ş. PEI N-doped graphene quantum dots/p-type silicon Schottky diode. *FlatChem.* **2022**, *36*, 36.
(51) Efil, E.; Kaymak, N.; Seven, E.; Orhan, E. O.; Bayram, O.; Ocak, S. B.; Tataroglu, A. Current−voltage analyses of Graphene-based structure onto Al2O3/p-Si using various methods. *Vacuum* **2020**, *181*, 109654.
(52) Kaymak, N.; Bayram, O.; Tataroğlu, A.; Bilge Ocak, S.; Oz Orhan, E. Electrical properties of Graphene/Silicon structure with Al2O3 interlayer. *J. Mater. Sci. Mater. Electron* **2020**, *31*, 9719−25.
(53) Nicollian, E. H.; Brews, J. R. *MOS (metal oxide semiconductor) physics and technology;* John Wiley & Sons, 2002.
(54) Hill, W. A.; Coleman, C. C. A single-frequency approximation for interface-state density determination. *Solid-State Electron.* **1980**, *23*, 987−93.
(55) Castagne, R.; Vapaille, A. Apparent interface state density introduced by the spatial fluctuations of surface potential in an m.o.s. *structure. Electron Lett.* **1970**, *6*, 691−4.
(56) Bilkan, Ç; Gümüş, A.; Altindal, Ş. The source of negative capacitance and anomalous peak in the forward bias capacitance-voltage in Cr/p-si Schottky barrier diodes (SBDs). *Mater. Sci. Semicond Process* **2015**, *39*, 484−91.

https://doi.org/10.1021/acsaelm.3c00011
ACS Appl. Electron. Mater. 2023, 5, 1804−1811